Chlorite chemical composition change in response to the Eocene-Oligocene climate transition on the northeastern Tibetan Plateau

Chengcheng Ye[a,b], Yibo Yang[a,c,*], Xiaomin Fang[a,b,c,*], Hanlie Hong[d], Chaowen Wang[e], Rongsheng Yang[a,b], Weilin Zhang[a,c]

[a] Key Laboratory of Continental Collision and Plateau Uplift, Institute of Tibetan Plateau Research, Chinese Academy of Sciences, Beijing 100101, China
[b] University of Chinese Academy of Sciences, Beijing 100049, China
[c] CAS Center for Excellence in Tibetan Plateau Earth Sciences and Chinese Academy of Sciences, Beijing 100101, China
[d] School of Earth Sciences, China University of Geosciences, Wuhan 430074, China
[e] Gemmological Institute, China University of Geosciences, Wuhan 430074, China

ARTICLE INFO

ABSTRACT

The Eocene-Oligocene climate transition (EOCT) at ~34 Ma is a pronounced environmental reorganization that occurred in the Cenozoic era and has been extensively studied via marine archives. However, to date, there is still a less well-dated continental record across the EOCT, which can mostly be attributed to a lack of suitable proxies used in the varied continental settings in terms of sedimentary facies, provenance and climate, thus resulting in a poor understanding of the continental response to this transition. Located on the northeastern Tibetan Plateau, the Qaidam Basin is filled with continuous and well-exposed Cenozoic fluvio-lacustrine sediments. Cenozoic lacustrine sediment has been proven to be an ideal archive to study the continental climatic response to the EOCT. Here, we present the detailed mineralogical and elemental composition of chlorite, a widespread clay mineral in continental sediments formed by rock weathering, collected from a lacustrine sequence in the northern Qaidam Basin to constrain the onset of the EOCT and the related climatic response. The results show that chlorite abundance, crystallinity indices, intensity ratios of chlorite diagnostic peaks and chemical composition collectively exhibit remarkable changes at ~34.3 Ma. To be more specific, the well-crystallized Fe-Mg-rich chlorites were characterized by a high Fe content before the EOCT and turned into high-Mg-content Mg-chlorites with poor crystallinity. The chlorite chemical composition change is assumed to have been related to regional drying after the EOCT, thus providing new insights into the continental paleoenvironmental change based on this novel proxy.

1. Introduction

The abrupt earth system shift from "greenhouse" to "icehouse" near the Eocene-Oligocene (E-O) boundary (ca. 34 Ma) has been of great interest in past decades. This Eocene-Oligocene climate transition (EOCT) is marked by the expansion of ice sheets in the Antarctic (Zachos et al., 2001; Coxall et al., 2005), accompanied by a series of dramatic changes, e.g., global sea-level drop (Katz et al., 2008; Miller et al., 2008), decline of the atmospheric CO_2 concentration (Pearson et al., 2009; Pagani et al., 2011) and biotic reorganization (Meng and McKenna, 1998; Pearson et al., 2008). However, the existing EOCT records mostly focused on its onset and duration using marine archives (Zachos et al., 1996; Coxall et al., 2005; Pearson et al., 2008; Scher et al., 2011), while a few archives of continental responses have been retrieved in North America (Wolfe, 1992; Retallack, 1992; Prothero,

1999; Zanazzi et al., 2007) and Europe (Cavagnetto and Anadón, 1996; Blondel, 2001; Costa et al., 2011; Hren et al., 2013). Recently, a growing number of EOCT records have been reported in central Asia and the northern Tibetan Plateau, e.g., Xining Basin (Dupont-Nivet et al., 2007; Chen, 2009; Xiao et al., 2010; Zhang and Guo, 2014), Tarim Basin (Wang et al., 2013), Junggar Basin (Zhang et al., 2012; Sun et al., 2014) and Lanzhou Basin (Zhang, 2015). However, some of these records are poorly constrained in age (Wang et al., 2013; Zhang et al., 2012; Sun et al., 2014), while the others exhibit remarkable uncertainty in proxy interpretation, especially in this tectonically active continental setting with varied sedimentary facies, provenance and climate (Dupont-Nivet et al., 2007; Xiao et al., 2010; Zhang and Guo, 2014; Zhang, 2015; Bush et al., 2016).

Most widely used climatic proxies in modern settings cannot be directly applied to long-term paleoclimate reconstruction using basin

sediments (Ye et al., 2016). Clay minerals are the weathering products that are mainly controlled by regional climate change and the parent rock (Chamley, 1989). Specifically, chlorite and illite are generally dominated in a typical physical weathering regime with a cold and arid environment (Chamley, 1989) and are therefore useful proxies with which to acquire the climate change information in this dramatic continental cooling event. However, diagenetic illite products, the illite/smectite mixed layer (I/S), are more common in long-term sedimentary sequences in the northern Tibetan Plateau, while chlorite diagenesis has been rarely reported (Hong et al., 2010; Wang et al., 2011; Zhang and Guo, 2014). As a result, chlorite seems to be one of the most appropriate clay mineral proxies with which to define continental climate change in response to the onset and the process of the EOCT in this region.

Here, we present detailed geochemical and mineralogical investigations of chlorite collected from a lacustrine interval (with a thickness of between 1400 and 2300 m) in the Hongliugou (HLG) section in the northern Qaidam Basin on the northeastern Tibetan Plateau to define the onset of the EOCT and associated climate evolution. The studied interval (40.5–31.0 Ma) covers a long period across the EOCT, thus proving a rare opportunity to constrain the onset of the EOCT and its climatic response on the northern Tibetan Plateau.

2. Geological setting

The Qaidam Basin is the largest intermontane basin (~700 km × 300 km) on the northeastern Tibetan Plateau. It is bounded by the Altyn Tagh fault in the northwest, the Qilian Shan-Nan Shan thrust belt in the northeast and the Eastern Kunlun transpressional system in the south (Yin et al., 2008; Fig. 1B). These large boundary faults between Qaidam Basin and those highly uplifted surrounding mountains therefore controlled the high relief contrast between them. The average elevations of the Qaidam Basin are mainly between 2500 and 3000 m above sea level (asl), while the elevations of the surrounding large mountain ranges are generally between 4000 and 5000 m asl. The rain shadows produced by these high mountains make the western basin one of the most arid areas in inland Asia, while the

southeastern basin is less arid due to moisture input from the Indian and East Asian monsoons (Chen et al., 2008; Luo et al., 2017; Nie et al., 2017). The mean annual precipitation (MAP) presents a decrease from 100 mm in the east to < 20 mm in the west. This MAP pattern also exerts influence on the vegetation distribution, from desert steppe in the east to desert in the west.

The Qaidam Basin is filled with Cenozoic sediments with a maximal thickness of ~12,000 m, receiving the large amounts of detritus produced from active thrust tectonics and erosion since the Paleocene (Song et al., 2013). The HLG section is well exposed at 38°07.50′ N, 94°41.07′ E and constrained by the north and south faults of Sertengshan in the northern margin of the basin. The HLG section covers a total thickness of 5030-m of continuous Cenozoic sediments from the early-middle Eocene Lulehe Formation to the late Pliocene-Pleistocene Shizigou Formation upwards. This upward sequence is precisely dated by high-resolution magnetostratigraphy and macrofossils and covers a period of 54–1.8 Ma (Zhang, 2006). The studied interval from the Xiaganchaigou Formation (1400–2300 m thick) mainly consists of brownish red, gray-green and purplish clayey siltstones, sandy siltstones, and sandstones deposited in shallow to semi-deep lacustrine environments (Fig. 2). The magnetostratigraphy model of studied interval covers six reversed (C12r, C13r, C15r, C16r, C17r and C18r) and five normal (C13n, C15n and C16n, C17n and C18n) polarity zones, yielding a depositional age range of 40.5–31.0 Ma (Zhang, 2006; Fig. 2). The thickness-to-age transformation of studied interval was calculated by linear interpolation between polarity transitions (Fig. 2).

3. Materials and methods

3.1. Clay mineral extraction and XRD analyses

The studied lacustrine interval of the HLG section contains a very low percentage (20% on average) of clays, while quartz, calcite, albite, and K-feldspar collectively make up ~80% of the bulk sample, as shown by X-ray diffraction (XRD) analysis of six siltstone-sandstone bulk samples (Ye et al., 2016). Here, < 5 μm clay fraction was employed in this study because of the enrichment of chlorite in coarser fraction
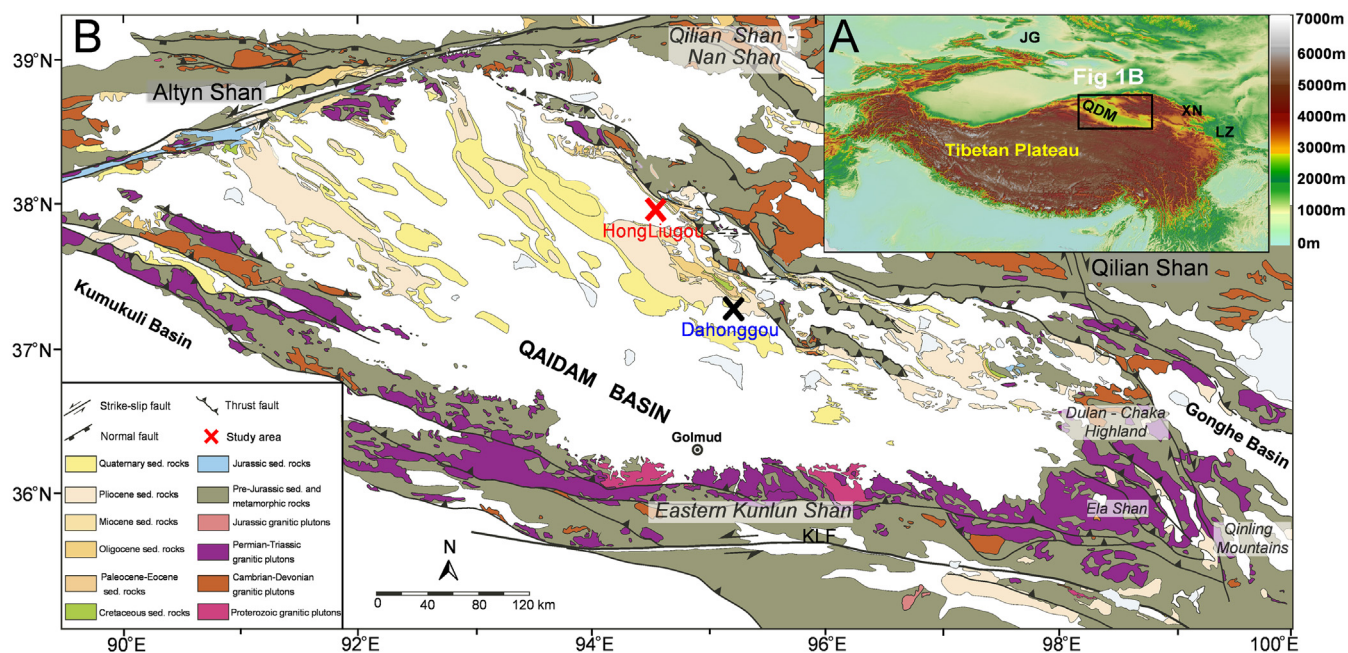

Fig. 1. (A) The location of the Qaidam Basin and related region in this study. Here, JG is short for Junggar Basin; QDM represents Qaidam Basin; XN is the abbreviation of Xining Basin and LZ is Lanzhou Basin. (B) Geologic map that specifies very detailed rock types of the Qaidam Basin (modified from Bush et al., 2016). The location of the Hongliugou (HLG) section is marked by a red cross. (For interpretation of the references to color in this figure legend, the reader is referred to the web version of this article.)
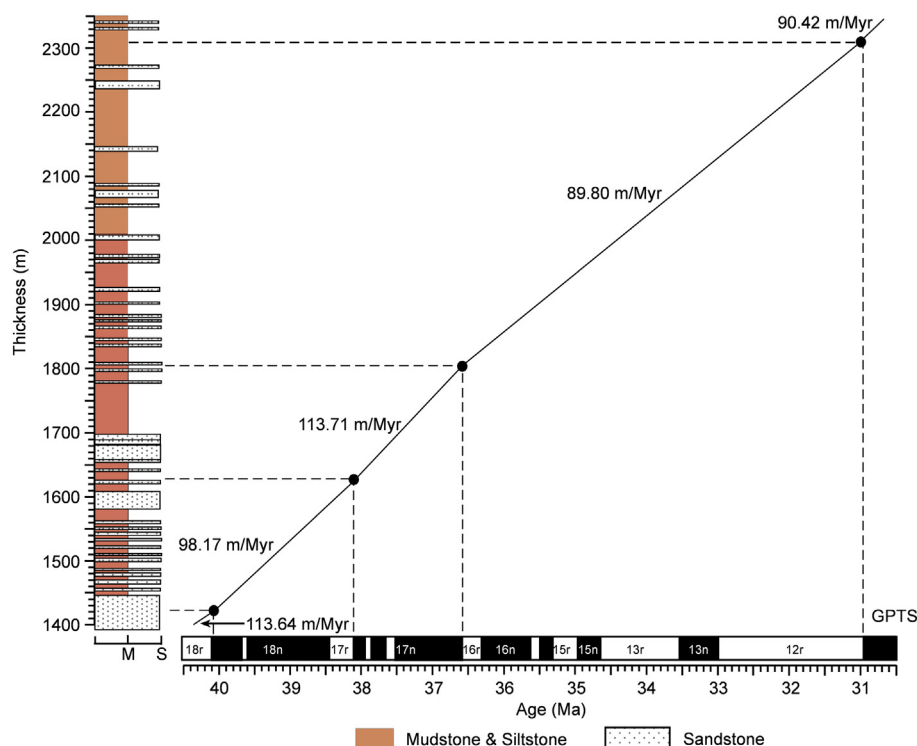
Fig. 2. Age versus depth plot of the studied interval in the HLG magnetostratigraphy sequence (Zhang, 2006) using the GPTS time scale (Cande and Kent, 1995).

(Gibbs, 1977; Johnson and Kelley, 1984). Gravitational sedimentation was used to isolate < 5 μm clay fraction in this study. In brief, approximately 50 g of bulk sample was weighted and organic matter and calcite therein were removed in advance by excess 25% H_2O_2 and 1 M acetic acid (HOAc). The air-dried, oriented clay mineral aggregates prepared by the glass slide method were analyzed on a Rigaku D/MAX-2000 diffractometer (Cu, Kα, 1.5406 Å, 40 kV, 100 mA, 3–30°, step 0.02°, 10°/min) at the Micro Structure Analytical Laboratory, Peking University. Then, the air-dried, oriented clay glass slides were further treated with ethylene glycol vapors for 24 h and heated to 450 °C for 2 h to obtain corresponding glycol-saturated (EG) and heated (T) diffractograms, respectively.

Chlorite was identified by the position of the (00l) series of basal reflections in diffractograms of the three states (air-dried (AD), glycol-saturated (EG) and heated (T)) for each sample on Jade 6.5 software (Fig. 3A, B). The diagnostic peaks of chlorite are 14.2 Å (001), 7.1 Å (002), 4.76 Å (003) and 3.54 Å (004). These even-order chlorite peaks (7.1 Å (002) and 3.54 Å (004)) nearly superimpose on the peaks of the kaolinite 00l series (7.1 Å (001) and 3.58 Å (002)), introducing difficulty in chlorite identification. In this study, we therefore use the odd-order chlorite peaks to distinguish these two clay minerals. In addition, as chlorite becomes dissolved in hot hydrochloric acid (HCl), it may also be applied to check for the presence of kaolinite in mutual mixtures.

A semi-quantitative estimate of chlorite was obtained by peak (7 Å) areas and heights of the basal reflections following SYT 5163-2010 (Zeng et al., 2010). The relative amounts of kaolinite and chlorite were further separated by the peak height ratios of 3.58/3.54 Å. The full width at half maximum (FWHM) of (Δ°2θ) at ~14.2 Å, 7.1 Å and 4.76 Å peaks on EG diffractograms is expressed as chlorite crystallinity (Chamley, 1989; Árkai, 1991; Árkai and Ghabrial, 1997; Wang et al., 2018). The presence of illite-smectite mixed layers (I/S) and kaolinite would distort the identification of $FWHM_{14.2Å}$ and $FWHM_{7.1Å}$; in this case, the chlorite crystallinity of those samples with undetectable kaolinite (n = 71) were read from the deconvolution of XRD diffractograms (Fig. 3C, with an angle range of 3–20° (Δ°2θ), Cu, Kα) using JADE 6.5.

Chlorite polytype identification was employed to determine its origin in this study. However, the diagnostic peaks of chlorite are mainly distributed in the range of 33–38° (Δ°2θ), which will be masked by the presence of illitic clay minerals due to the overlap of the diagnostic chlorite peaks. Therefore, to eliminate the effect of illitic clay minerals, we determined chlorite polytypes following Hillier (1993). In brief, the difference of two unoriented diffractograms (one from the original sample and the other from hot HCl leached sample) are applied for chlorite polytype identification (Fig. 4A), during which hot HCl is used to dissolve chlorite (Moore and Reynolds, 1989).

3.2. Chemical analyses

To characterize the chemical composition of chlorite, forty-six chlorite-bearing clay samples were further oven dried and treated with hot hydrochloric acid (HCl). Approximately 0.5 g of powdered samples was weighed into 15 ml polyethylene centrifuge tubes and then treated with 10 ml of 2 M HCl at 80 °C. To assess the effect of the reaction time on the chlorite dissolution, we first performed a dissolution test with a varied reaction time for 2 and 4 h. The XRD diffractograms of both acid residues indicate that 2 h and 4 h of heating treatments resulted in indistinctive differences (Fig. 5); thus, a heating time of 2 h was chosen in this study. Supernatants were collected after centrifugation (3600 rpm) and then diluted for major element (Al, Mg, and Fe) analyses with a Leeman Labs Prodigy-H inductively coupled plasma optical emission spectrometer (ICP-OES) at the Institute of Tibetan Plateau Research, Chinese Academy of Sciences (ITP-CAS), Beijing. All major element concentrations were normalized to the weight of the oven dried samples with relative standard deviations (RSDs) of the replicate analyses of < 2%.

To characterize the provenance information, trace elements (Th, Sc, Cr and Zr) of the clay fraction digested by pressurized acid digestion using a mixture of HNO_3 and HF, following Yang et al. (2013). In brief, approximately 20–30 mg of oven-dried clay sample material was weighed into a Teflon container and then digested with a mixture of 1 ml concentrated HNO_3 (CMOS, JT. Baker, USA) and 1 ml
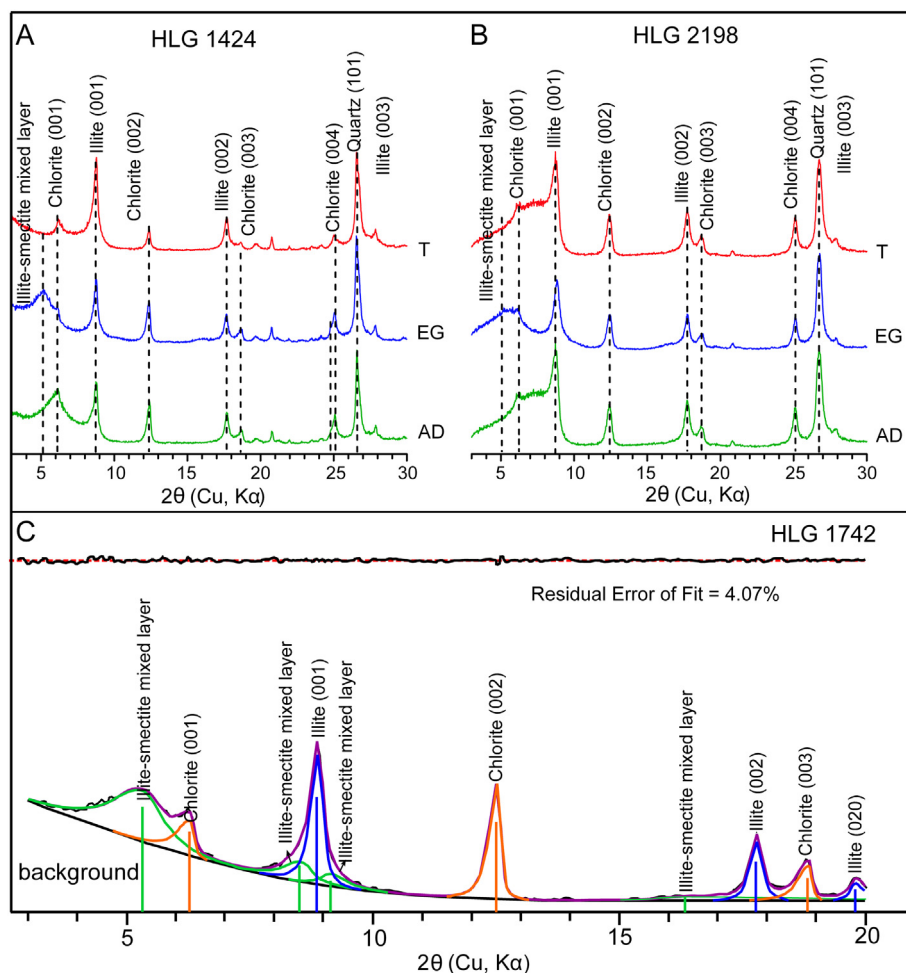
Fig. 3. XRD patterns of two representative clay samples in the HLG section. (A) Sample from 1424 m with a typical illite/smectite mixed layer (I/S), illite, chlorite and kaolinite. (B) Sample from 2198 m with a typical irregular illite/smectite mixed layer (I/S), illite, chlorite and undetectable kaolinite. AD: air-dried sample; EG: glycol-saturated sample; T: heated sample. (C) Deconvolution of XRD patterns (Cu, Kα) from a sample at a depth of 1742 m with an angle range of 3–20° (Δ°2θ). The residual error of fit should be < 5% in the deconvolution.
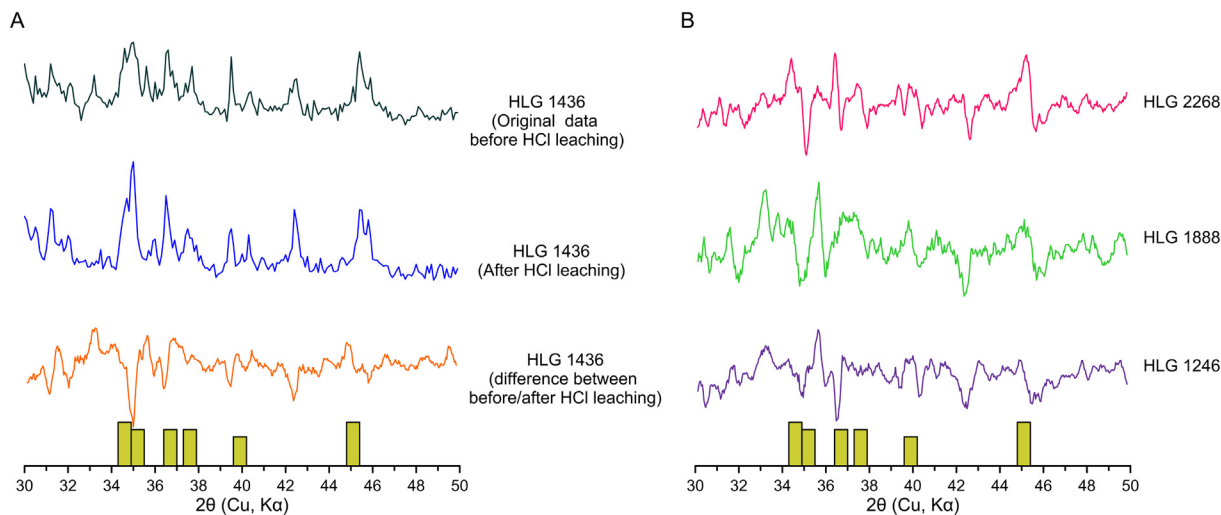
Fig. 4. Randomly oriented powder XRD patterns of the < 5 μm fraction after HCl dissolved for chlorite polytypes identification. (A) Schematic diagram showing the chlorite polytypes obtained from differences between original and HCl dissolved diffractograms. (B) Three representative clay samples for polytype identification in the studied lacustrine interval. The yellow vertical bars mark positions and relative intensities of diagnostic IIb peaks after Brown and Bailey (1962). The curves denote 7-point running averages of the raw data. (For interpretation of the references to color in this figure legend, the reader is referred to the web version of this article.)
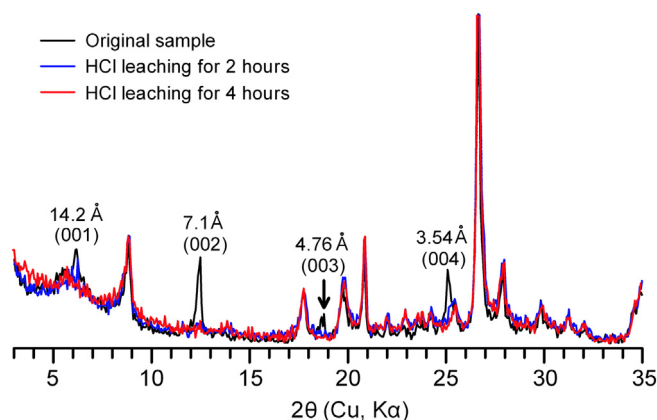
Fig. 5. Randomly oriented powder XRD patterns of the original and hot HCl dissolved clay samples (< 5 μm) with different time intervals. The results indicate that chlorite is the only component to be dissolved.

concentrated HF (BVIII, Beijing Institute of Chemical Reagent Research, P. R. China). After treating in an ultrasonic bath for 20 min, the mixture was further digested in an oven for 24 h at 190 °C. The cooled solution in the last step was then dried at 150 °C, after which HNO_3 was added to the residue and repeatly heated at 150 °C for 24 h. Finally, the trace elements of ultra-pure water diluent digestant were further determined by ICP-MS (X-7; Thermo-Elemental, USA) at the ITP-CAS. All results are reported in parts per billion (ppm) with relative standard deviations (RSDs) of the replicate analyses that were < 5%.

3.3. Micromorphological analyses

Representative chlorite-enriched samples were selected to study their morphological features (e.g., texture and particle size). The bulk samples were mounted onto stubs with conductive resin and then sputter-coated with a thin conductive layer of platinum-palladium before SEM observations. The analysis was then undertaken at the School of Materials Science and Engineering, University of Science and Technology of Beijing, China, using FEI Quanta 450 FEG scanning electron microanalyzer (SEM) at an accelerating voltage of 0.2–20 kV. The relative element contents of selected chlorite particles during observation were determined by an energy-dispersive X-ray spectroscopy (EDS) system (Quantax 200 with X-Flash-Bruker).

4. Results

4.1. Clay minerals

The clay mineral assemblages in the studied part of the HLG section mainly consist of illite-smectite mixed layers, illite, chlorite, kaolinite (Fig. 3A, B). The most abundant clay mineral in HLG section is illite-smectite which occupies 0%–90% (average 56%) of the total clay minerals. The average abundance of illite is 29%. The chlorite mineralogical characters in the studied interval are presented in Fig. 6A–F. The chlorite content varies within wide limits, from 1% to 20%, with an average of 11% (n = 103). Specifically, the content of chlorite remains low, with values (average 10%, n = 73) from the bottom to approximately 2004 m (~34.3 Ma in age) and then starts to increase upwards to the top of the Xiaganchaigou Formation, with an average of 13% (n = 30) (Fig. 6A). The chlorite relative abundance, defined as the height ratio between chlorite (003) and illite (002) diagnostic peaks (Chamley, 1989), exhibits similar secular change with chlorite content characterized by higher values between 2004 and 2300 m (average 0.65, n = 30) than those (average 0.56, n = 73) between 1400 and 2004 m (Fig. 6B). Chlorite crystallinity indices expressed as the FWHM at ~14.2 Å ($FWHM_{14.2Å}$), 7.1 Å ($FWHM_{7.1Å}$) and 4.76 Å ($FWHM_{4.76Å}$)

show similar secular trends with chlorite content in the studied interval (Fig. 6C–E). Chlorite crystallinities show relatively low values from the bottom to a depth of approximately 2004 m, with an average of 0.378 for $FWHM_{14.2Å}$ (n = 43), 0.294 (n = 43) for $FWHM_{7.1Å}$ and 0.359 (n = 43) for $FWHM_{4.76 Å}$; then, they increase upward greatly until the top of the Xiaganchaigou Formation, with an average of 0.867 (n = 28), 0.335 (n = 28) and 0.445 (n = 28) for $FWHM_{14.2Å}$, $FWHM_{7.1Å}$ and $FWHM_{4.76 Å}$, respectively. The intensity ratios of different chlorite diagnostic peaks are also presented in Fig. 6F. Secular trends of intensity ratios between chlorite the second and the first diagnostic peaks (defined as Int(002)/Int(001) in the following) vary remarkably with a range of 0.54–3.70. The intensity ratios between chlorite the third and the first diagnostic peaks (defined as Int(003)/Int(001) in the following) also exhibit similar secular change with Int(002)/Int(001), varying from 0.23 to 1.67. Moreover, both these Int(002)/Int(001) and Int(003)/Int(001) display similar changes to the curve of $FWHM_{14.2Å}$ (Fig. 6C), $FWHM_{7.1Å}$ (Fig. 6D) and $FWHM_{4.76Å}$ (Fig. 6E).

4.2. Major elements

Two ratios (Fe/(Fe + Mg) and Mg/Al) in HCl leachates are presented in Fig. 6H and I. Fe/(Fe + Mg), a parameter widely used to evaluate the Fe enrichment in chlorite, presents an obviously decreasing secular trend from a thickness of 1400 m, with high values of 0.57–0.69 (average 0.63, n = 32) to 2004 m and low values of 0.49 to 0.66 (average of 0.58, n = 14) (Fig. 6H). The Mg/Al ratios display similar changes to Fe/(Fe + Mg) and remain low, with values averaging 0.92 (ranging from 0.78 to 1.14, n = 32) in the interval of 1400–2004 m, and then increase upward with a mean of 1.06 (ranging from 0.79 to 1.37, n = 14) (Fig. 6I).

5. Discussion

5.1. Origin of chlorite

The origin of chlorite can be determined by chlorite polytypes. The results show that chlorites in the studied interval are mainly the IIb polytype, as indicated by the existence of diagnostic IIb peaks (Fig. 4A, B), and this type of chlorite is distributed widely in continental settings (Brown and Bailey, 1962). The occurrence of clay-sized IIb chlorite in unmetamorphosed sediments is proven to be of detrital origin, while Ib chlorite in sediments is authigenic/diagenetic (Hayes, 1970). The detrital origin of chlorite in the studied interval is further supported by the micromorphological features (Fig. 7A). The chlorite identified by a chemical composition of Si, Al, Mg and Fe (Fig. 7B) generally occurs in poorly developed plates with irregular outlines or ragged edges. Moreover, the uneven basal (001) planes of chlorite crystals associated with well-developed fissures (Fig. 7A) further suggest that the detrital chlorite has undergone intensive stripping and impaction during the transport process (Hong et al., 2007). Therefore, chlorite in the studied interval was originated from catchment weathering and has not been subjected to further diagenesis. The chlorite of detrital origin may be derived from Qilian Shan–Nan Shan according to the detailed provenance study of contemporaneous sediments from Dahonggou section (Fig. 1B), which is < 100 km southeast away from the Hongliugou section (Bush et al., 2016).

5.2. Chlorite chemical composition change across the EOCT

Chlorite $((R_xAl_{6-x})(Si_yAl_{4-y})O_{10}(OH)_8)$ is a typical hydrous silicate and consists of a 2:1 layer plus a brucite-liked interlayer sheet in structure. The commonly seen chlorites are Mg- and Fe-dominant species, during which there is a continuous solid solution series between Mg and Fe species (Bailey, 1988). Replacements of Mg by Fe is a common type of ionic replacement (Foster, 1962) and occurs in octahedral sites involving a 2:1 octahedral sheet, as well as an interlayer
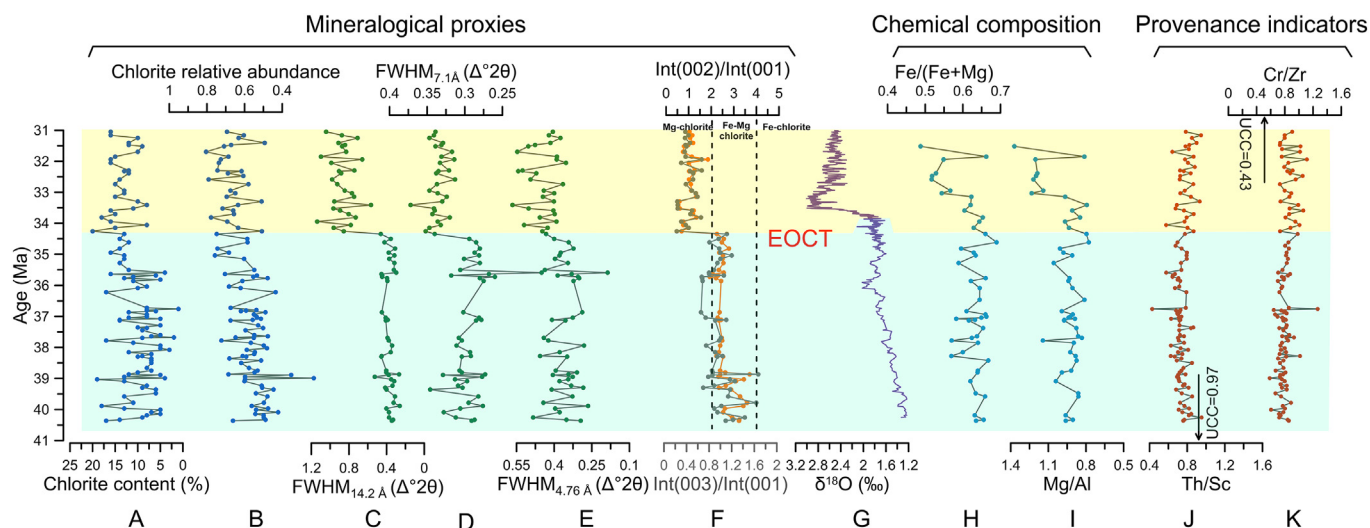
Fig. 6. Secular changes of chlorite mineralogical and chemical compositions. (A) Chlorite content (%); (B) chlorite relative abundance (height ratio of 4.76 Å/5 Å); (C) full width at half maximum (FWHM) at chlorite 14.2 Å; (D) FWHM at chlorite 7.1 Å; (E) FWHM at chlorite 4.76 Å; (F) intensity ratios of different chlorite peaks; (G) marine benthic oxygen isotopes (Zachos et al., 2001). (H) Fe/(Fe + Mg) ratios from HCl leaching; (I) Mg/Al ratios from HCl leaching; (J–K) provenance indicators showing the contribution of mafic/felsic minerals.

sheet (Bailey, 1988). This replacement would lead to a decrease in the intensity of the particular chlorite reflections since Fe generally has a diffracting power that is twice as large as that of Mg (Petruk, 1964). Therefore, the increase in Fe substitution in chlorite would cause a weakening of odd-order (001, 003 and 005) reflections relative to even-order (002 and 004) reflections (Moore and Reynolds, 1989). The decrease of chlorite Int(002)/Int(001) after the EOCT in our study thus suggests a decrease of Fe content in chlorite since that time. This is further supported by the decrease in Fe/(Fe + Mg) and the increase in Mg/Al during HCl leachates (Fig. 6H, I). Here, the Fe/(Fe + Mg) and Mg/Al ratios in HCl leachates can be used as proxies in determining chlorite chemical composition because the highly correlated Fe, Mg and Al suggest that they are dissolved mainly from the chlorite (Fig. 8A–D) and the XRD shows only the disappearance of chlorite peaks (Fig. 5). Moreover, the decrease of Fe content in the brucite-liked interlayer sheet would reduce the intensity ratios of 003/001 and 003/005 reflections, while the reverse effect is produced by the decrease of Fe in the silicate layer (Moore and Reynolds, 1989). Similar secure trends and the highly positive correlation between chlorite Int(002)/Int(001) and Int(003)/Int(001) (Fig. 6F and Fig. 9B) therefore collectively indicate a decrease Fe substitution is mainly occurring in the brucite-like interlayer sheet after the EOCT, thus yielding an increase in the Mg content in chlorite.

The different diffractogram patterns of the chlorite subgroups make it possible to use the ratio of different chlorite reflections to distinguish different chlorite subgroups. In brief, Mg-rich chlorites generally display five stronger basal reflections, while Fe-rich chlorites present strong even-order and weak odd-order basal reflections (Wilson, 1987). Therefore, the intensity ratio of chlorite 002 and 001 peaks (Int(002)/Int(001)) is also employed in chlorite subgroup identifications. The Mg-rich chlorites have Int(002)/Int (001) < 2, and Fe-Mg-rich chlorite has an Int(002)/Int(001) range of 2–4 (Carroll, 1969). The chlorite Int (002)/Int(001) in the studied interval overall displays a decreasing trend with a range of 0.54–3.70 (Fig. 6F). Therefore, we propose that two chlorite subgroups existed in the studied interval; that is, Fe-Mg-rich chlorites were the dominant species before the EOCT, while Mg chlorites became more abundant after the EOCT. The dominant subgroup changed across the EOCT, therefore also reflecting the higher Fe content before the EOCT and the higher Mg content after the EOCT (Fig. 6H, I).

The above interpretation can be tested by Fe substitution impact on crystallinity change. The negative correlation between chlorite crystallinity and intensity ratios of different chlorite diagnostic peaks (Fig. 9C, D) therefore clearly indicates that changes in chemical composition do significantly affect the half-height width of the basal reflection of chlorite. As a result, the chlorite crystallinity increases after
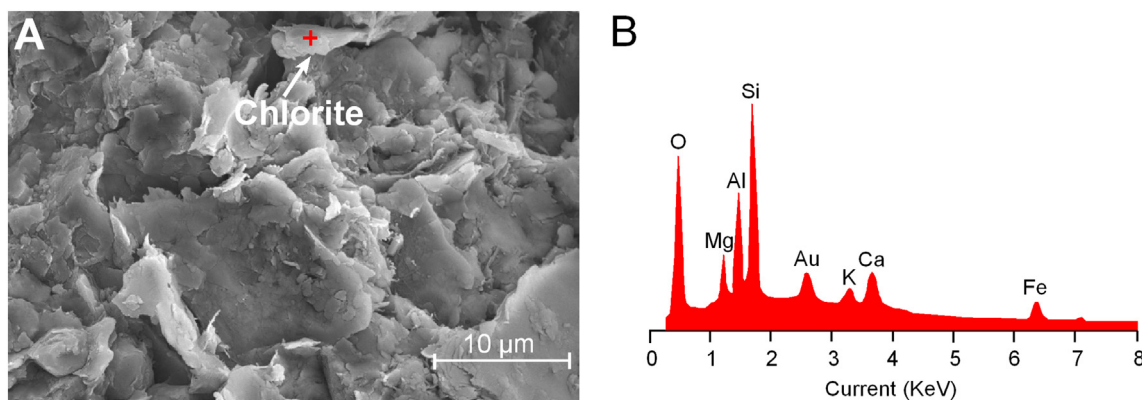
Fig. 7. SEM images showing the micromorphological features of chlorite. (A) Chlorite mainly occurs as poorly developed plates with irregular outlines or ragged edges. (B) EDS analysis of a selected area marked by a red cross in (A). (For interpretation of the references to color in this figure legend, the reader is referred to the web version of this article.)
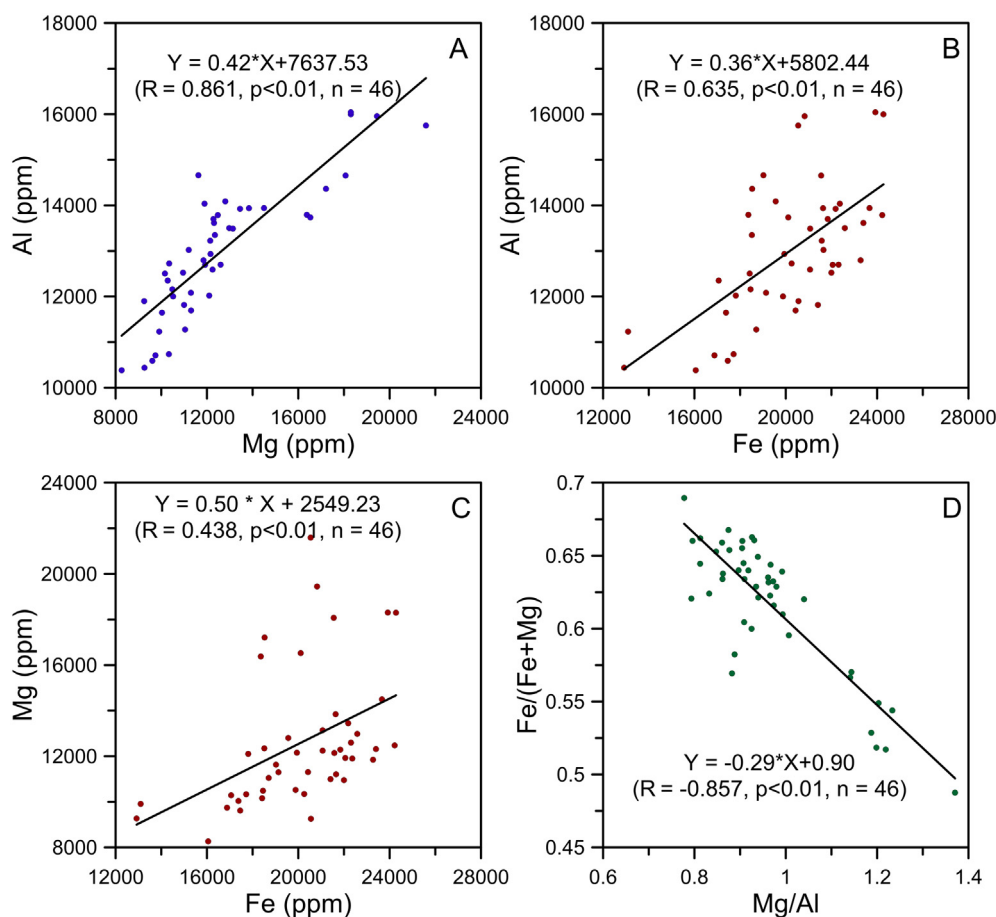
Fig. 8. Correlation analyses of major elements in HCl leachates.

the EOCT can also reflect the Fe content decrease in chlorite (Fig. 6C–E).

The chlorite diagnostic peaks intensity ratios (Int(002)/Int(001), Int(003)/Int(001)), crystallinity indices and wet chemical analysis results collectively suggest chlorite Fe content decrease after the EOCT. The variations in the Mg and Fe contents in the chlorite chemical composition are theoretically strongly dependent on the geological environment and consequently on the Fe-Mg relative proportion (Fe/Mg ratios) in the source rock and parent solution composition during chlorite formation (Cathelineau, 1988). The change in solution composition is regulated by both provenance and climate, as well as and the solution property influencing Fe substitution mainly in the hydroxide layer.

The Fe/Mg ratio in the parent rocks at the source area is the primary provenance factor controlling the chlorite chemical composition. As a globally averaged mineral mixing product, the classic mafic lower continental crust and felsic upper continental crust (UCC) are characterized by distinct Fe/Mg ratios (Fe/Mg = 1.18, for the lower continental crust, Rudnick and Fountain, 1995; Fe/Mg = 2.05, for the upper continental crust, Taylor and McLennan, 1985), suggesting that the relative contribution of mafic/felsic minerals should be considered. Scandium (Sc) is generally enriched in mafic rocks, and thorium (Th) is mainly derived from felsic rocks. They are geochemically insensitive to chemical weathering, and their ratios exhibit negligible alteration during transport and sedimentary processes. Th/Sc is thus a widely used provenance indicator to determine the contribution of felsic/femic minerals (Taylor and McLennan, 1985). Moreover, another independent ratio Cr/Zr is also employed as an indicator to evaluate contribution of mafic/felsic minerals, as Cr is abundant in mafic rocks and Zr is richer in felsic rocks (Wronkiewicz and Condie, 1987). Th/Sc ratios and Cr/Zr ratios of the clay fraction of studied intervals

collectively display a steady trend with limited variability, implying negligible changes in provenance (Fig. 6J, K). However, as Zr also tends to be enriched in the coarse fraction (Chen et al., 2006), our study thus exhibits overall higher Cr/Zr ratios in the clay fraction than those in the UCC composition (Fig. 6K). Meanwhile, these two provenance indicators could also be employed to evaluate the impact of tectonics on the paleoenvironment. Tectonic rejuvenation would allow virtually the exposure of various parent rocks and lead to a strong diversification of eroded materials (Chamley, 1989). The negligible changes in provenance and stable sedimentary facies with constant sedimentation rates (Zhang, 2006, Fig. 2) in 35.4–30.5 Ma therefore suggest that tectonics may play a minor effect on regional climate change across EOCT.

As the parent rock composition generally remains steady and the impact of tectonic on regional climate change is minor, the decrease in Fe content and increase in Mg in chlorite after the EOCT may therefore be related to the climate-forced Mg-rich process in parent solutions. Previous studies have shown that Mg-rich chlorites are characteristically found in more evaporitic conditions where the sufficiently high Mg concentration derived from evaporitic and alkaline conditions is favorable for Mg-chlorite formation (Weaver, 1989). In addition, during the weathering process under alkaline conditions the Mg-rich brucite sheet tended to be less stripped out and removed from the immediate environment and the process of Fe substitution was thus less pronounced (Weaver and Pollard, 1973). This Mg-rich and alkaline condition is much more plausible, as evidenced by a more drying and cooling climate after the EOCT.

5.3. Implications

Such distinct changes in chlorite content and relative abundance
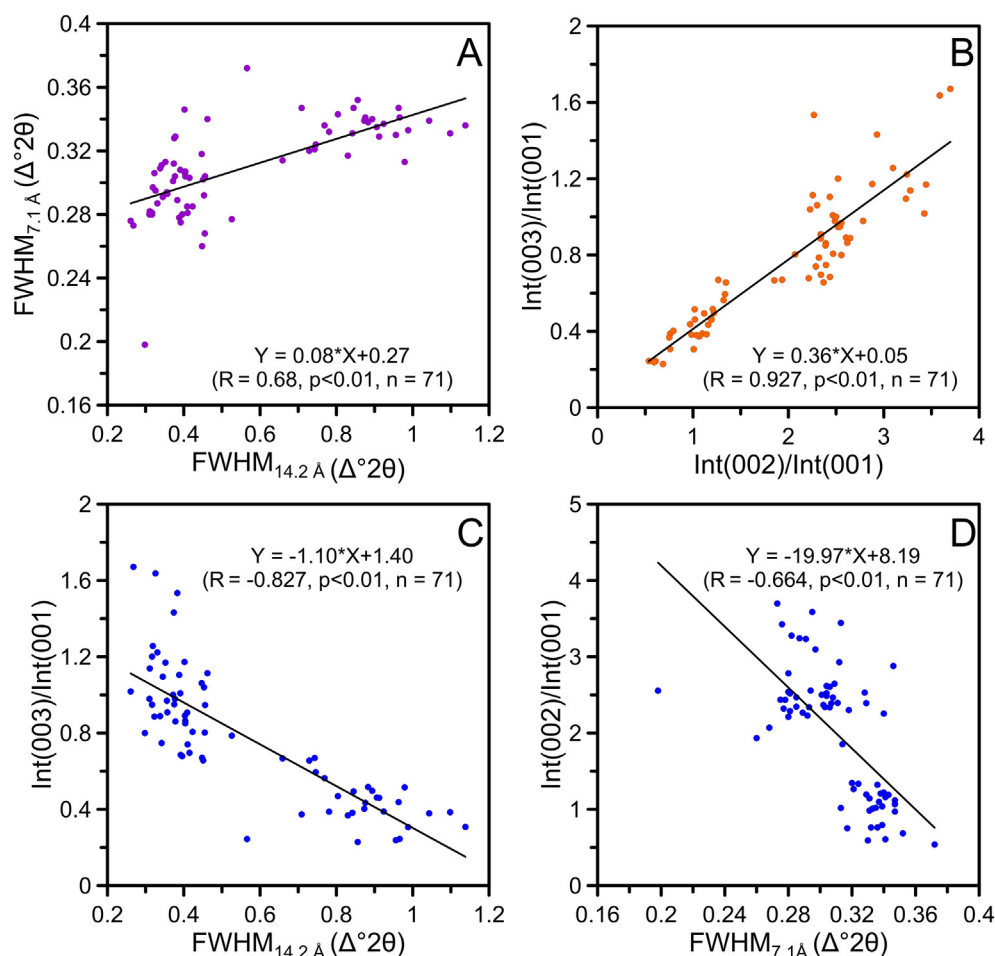
Fig. 9. Correlation analyses of different proxies for chlorite chemical composition. (A) Chlorite crystallinities: crystallinity ($FWHM_{7.1Å}$ vs $FWHM_{14.2Å}$). (B) Chlorite intensity ratios: Int(003)/Int(001) vs. Int(002)/Int(001). (C) Int(003)/Int(001) vs. $FWHM_{14.2Å}$. (D) Int(002)/Int(001) vs. $FWHM_{7.1Å}$.

(Fig. 6A, B) crystallinity indices (Fig. 6C–E), diagnostic peaks intensity ratios (Fig. 6F) and chemical composition (Fig. 6H, I) at 34.3 Ma in the Xiaganchaigou Formation thus could be reasonably attributed to a regional climate response of the EOCT in the Qaidam Basin, which is further confirmed by the decrease in sediment redness in the HLG section (Han, 2008). The sediment redness with clear climatic significance is often related to the fine-grained hematite content (Nie et al., 2010), and thus, a decrease in redness suggests less hematite formation during deteriorated water-heat conditions and vice versa (Fang et al., 1999; Hu et al., 2014).

Indeed, the chlorite-derived EOCT record in the Qaidam Basin is generally consistent with other dramatic environmental changes at approximately 34 Ma in adjacent regions (see their locations in Fig. 1A). For example, an aridification event shown by the disappearance of gypsum/mudstone alternations in the Shuiwan section at ~34.0 Ma was recognized in the Xining Basin (Dupont-Nivet et al., 2007). Pollen records in the Xiejia section (Chen, 2009) (Fig. 10C) and clay mineral assemblages (Zhang and Guo, 2014) associated with sediment redness in the neighboring Tashan section (Xiao et al., 2010) (Fig. 10D, E) further confirmed this cooling and drying event approximately 33.9–34.1 Ma in the Xining Basin. This climatic deterioration is also identified in the neighboring Lanzhou Basin, as indicated by the higher Na/Al and lower hematite/goethite ratios, which implies weakened chemical weathering during cooling and drying conditions after 33.9 Ma (Fig. 10F, G) (Zhang, 2015). The abrupt replacement of large-size perissodactyl faunas in forests under a warm-temperate climate by small rodent/lagomorph-dominant faunas in forest-steppes in a dry-temperate climate in the Junggar Basin has been reported at 33.9 Ma

(Fig. 10H) (Zhang et al., 2012). This is also supported by another study in the Junggar Basin during which the decrease in kaolinite content and flora turnover from a warm-humid forest to a dry-temperate forest-steppe at ~34 Ma indicate a cooling and drying trend (Sun et al., 2014) (Fig. 10I–K).

The chlorite-derived drying and cooling climate in the Qaidam Basin and the abovementioned records in adjacent regions collectively exhibit a board regional cooling and drying response to the EOCT at the northern Tibetan Plateau. The regional drying trend may be related to an abrupt temperature decrease after the EOCT. The northern Tibetan Plateau is still in the subtropical hot-dry zone during the late Eocene-early Oligocene period (Sun and Wang, 2005), suggesting that the humid-arid fluctuations in the region are largely controlled by evaporation and precipitation. Therefore, the rapid temperature drop after EOCT may weaken the temperature-dependent evaporation in the moisture source, yielding less precipitation in this region (Gasse, 2000; Ye et al., 2016).

6. Conclusions

In this study, we performed an integrated investigation of chlorite mineralogical and geochemical characteristics from an Eocene-Oligocene lacustrine sequence in the northern Qaidam Basin. The significant changes in chlorite relative abundance, crystallinities, chemical composition and sediment color along the studied interval together constrain the EOCT response at ~34.3 Ma in the Qaidam Basin, which is coherent with adjacent region EOCT records in terms of the onset of the EOCT and the related climate evolution. The chlorite-derived drying
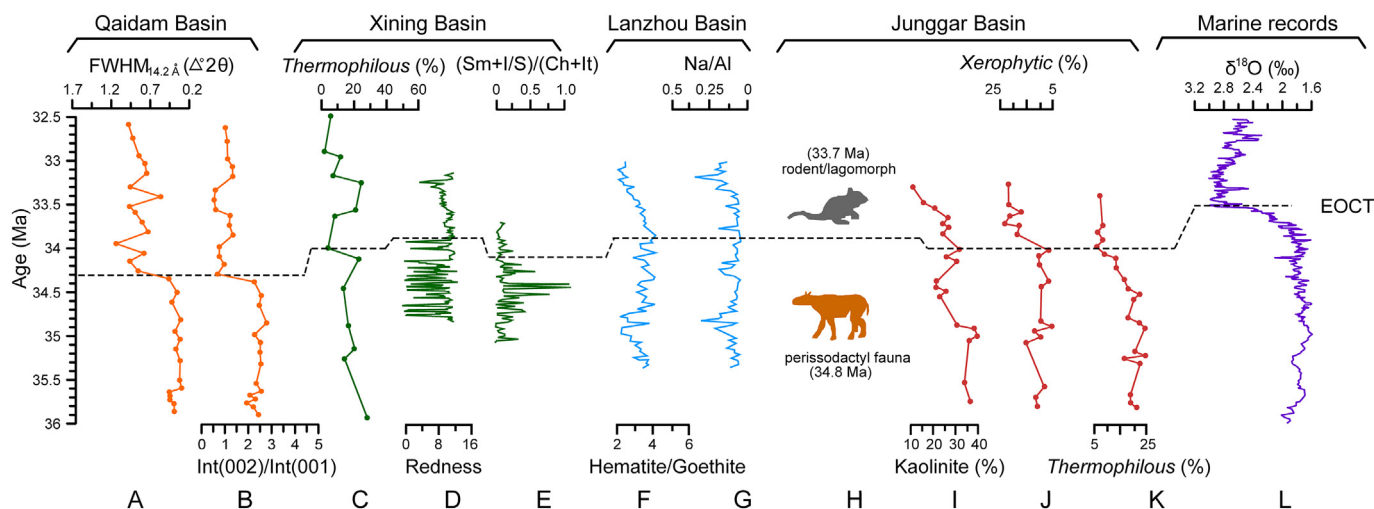
Fig. 10. Long-term integrated EOCT records from the Qaidam Basin and adjacent region. (A–B): Chlorite crystallinity and diagnostic peaks intensity ratios from this study. (C–E) Pollen assemblages (Chen, 2009), sediment redness (Xiao et al., 2010) and (smectite + I/S)/(chlorite + illite) ratios (Zhang and Guo, 2014) from the Xining Basin; (F–G) Na/Al and hematite/goethite ratios from the Lanzhou Basin (Zhang, 2015); (H–K) faunas fossils (Zhang et al., 2012), kaolinite content, xerophytic and thermophilous elements (Sun et al., 2014) from the Junggar Basin; (L) marine benthic oxygen isotopes (Zachos et al., 2001).

trend after the EOCT in the Qaidam Basin may be related to abrupt temperature declines, which weaken the temperature-dependent evaporation in the moisture source. This climate cooling and drying after the EOCT therefore exerts a great influence on chlorite geochemical composition, yielding a transition from well-crystallized Fe-Mg chlorite with a higher Fe content before the EOCT to the poor-crystallized Mg-chlorite with a higher Mg content after the EOCT. As chlorite is widespread in terrestrial sediments and has a relatively higher stability than other clay minerals during burial, this study has proven that chlorite chemical composition is a novel proxy in long-term continental paleoclimatic reconstruction.

Acknowledgments

References

Árkai, P., 1991. Chlorite crystallinity: an empirical approach and correlation with illite crystallinity, coal rank and mineral facies as exemplified by Palaeozoic and Mesozoic rocks of northeast Hungary. J. Metamorph. Geol. 9, 723–734.

Árkai, P., Ghabrial, D.S., 1997. Chlorite crystallinity as an indicator of metamorphic grade of low-temperature meta-igneous rocks: a case study from the Bükk Mountains, northeast Hungary. Clay Miner. 32, 205–222.

Bailey, S.W., 1988. Chlorites: structures and crystal chemistry. Rev. Mineral. Geochem. 19, 347–403.

Blondel, C., 2001. The Eocene-Oligocene ungulates from Western Europe and their environment. Palaeogeogr. Palaeoclimatol. Palaeoecol. 168, 125–139.

Brown, B.T., Bailey, S.W., 1962. Chlorite polytypism. I. Regular and semi-random 1-layer structures. Am. Mineral. 47, 819.

Bush, M.A., Saylor, J.E., Horton, B.K., Nie, J., 2016. Growth of the Qaidam Basin during Cenozoic exhumation in the northern Tibetan Plateau: inferences from depositional patterns and multiproxy detrital provenance signatures. Lithosphere 8, 58–82.

Cande, S.C., Kent, D.V., 1995. Revised calibration of the geomagnetic polarity timescale for the Late Cretaceous and Cenozoic. J. Geophys. Res. 100, 6093–6095.

Carroll, D., 1969. Chlorite in Central North Pacific Ocean Sediments. Proceeding of International Clay Conference. 1. Israel Universities Press, pp. 335–338.

Cathelineau, M., 1988. Cation site occupancy in chlorites and illites as function of temperature. Clay Miner. 23, 471–485.

Cavagnetto, C., Anadón, P., 1996. Preliminary palynological data on floristic and climatic changes during the Middle Eocene-Early Oligocene of the eastern Ebro Basin, northeast Spain. Rev. Palaeobot. Palynol. 92, 281–305.

Chamley, H., 1989. Clay sedimentology. Springer-Verlag, Berlin, Heidelberg, pp. 1–623.

Chen, C.F., 2009. Cenozoic Pollen Records and Palaeoenvironmental Evolution in Xining Basin, Northeastern Tibetan Plateau. Lanzhou University (Master's thesis).

Chen, J., Chen, Y., Liu, L., Ji, J., Balsam, W., Sun, Y., Lu, H., 2006. Zr/Rb ratio in the Chinese loess sequences and its implication for changes in the East Asian winter monsoon strength. Geochim. Cosmochim. Acta 70, 1471–1482.

Chen, F., Yu, Z., Yang, M., Ito, E., Wang, S., Madsen, D.B., Huang, X., Zhao, Y., Sato, T., Birks, H.J.B., Boomer, I., Chen, J., An, C., Wünnemann, B., 2008. Holocene moisture evolution in arid central Asia and its out-of-phase relationship with Asian monsoon history. Quat. Sci. Rev. 27, 351–364.

Costa, E., Garcés, M., Sáez, A., Cabrera, L., López-Blanco, M., 2011. The age of the "Grande Coupure" mammal turnover: new constraints from the Eocene–Oligocene record of the Eastern Ebro Basin (NE Spain). Palaeogeogr. Palaeoclimatol. Palaeoecol. 301, 97–107.

Coxall, H.K., Wilson, P.A., Pälike, H., Lear, C.H., Backman, J., 2005. Rapid stepwise onset of Antarctic glaciation and deeper calcite compensation in the Pacific Ocean. Nature 433, 53–57.

Dupont-Nivet, G., Krijgsman, W., Langereis, C.G., Abels, H.A., Sabbadini, R., Dai, S., Fang, X., 2007. Tibetan Plateau aridification linked to global cooling at the Eocene-Oligocene transition. Nature 445, 635–638.

Fang, X.M., Ono, Y., Fukusawa, H., Bao-Tian, P., Li, J.J., Guan, Dong-Hong, G., Oi, K., Tsukamoto, S., Torri, M., Mishima, T., 1999. Asian summer monsoon instability during the past 60,000 years: magnetic susceptibility and pedogenic evidence from the western Chinese Loess Plateau. Earth Planet. Sc. Lett. 168, 219–232.

Foster, M.D., 1962. Interpretation of the composition and a classification of the chlorites. US Geol. Surv. Prof. Pap. 414-A, 1–33.

Gasse, F., 2000. Hydrological changes in the African tropics since the Last Glacial Maximum. Quat. Sci. Rev. 19, 189–211.

Gibbs, R.J., 1977. Transport phases of transition metals in the Amazon and Yukon Rivers. Geol. Soc. Am. Bull. 88, 829–843.

Han, W.X., 2008. Climatic Records of Cenozoic Sediments From Qaidam Basin and Their Implications on Drying of Asian Inland. Lanzhou University (PhD thesis).

Hayes, J.B., 1970. Polytypism of chlorite in sedimentary rocks. Clay Clay Miner. 18, 285–306.

Hillier, S., 1993. Origin, diagenesis, and mineralogy of chlorite minerals in Devonian lacustrine mudrocks, orcadian basin, Scotland. Clay Clay Miner. 41, 240–259.

Hong, H., Li, Z., Xue, H., Zhu, Y., Zhang, K., Xiang, S., 2007. Oligocene clay mineralogy of the Linxia Basin: evidence for paleoclimatic evolution subsequent to the initial-stage uplift of the Tibetan Plateau. Clay Clay Miner. 55, 491–503.

Hong, H.L., Zhang, K.X., Li, Z.H., 2010. Climatic and tectonic uplift evolution since ~7 Ma in Gyirong basin, southwestern Tibet plateau: clay mineral evidence. Int. J. Earth Sci. 99, 1305–1315.

Hren, M.T., Sheldon, N.D., Grimes, S.T., Collinson, M.E., Hooker, J.J., Bugler, M., Lohmann, K.C., 2013. Terrestrial cooling in Northern Europe during the Eocene-Oligocene transition. Proc. Natl. Acad. Sci. 110, 7562–7567.

Hu, X.F., Du, Y., Guan, C.L., Xue, Y., Zhang, G.L., 2014. Color variations of the Quaternary Red Clay in southern China and its paleoclimatic implications. Sediment. Geol. 303, 15–25.

Johnson, A.G., Kelley, J.T., 1984. Temporal, spatial, and textural variation in the

mineralogy of Mississippi River suspended sediment. J. Sediment. Res. 54, 67–72.

Katz, M.E., Miller, K.G., Wright, J.D., Wade, B.S., Browning, J.V., Cramer, B.S., Rosenthal, Y., 2008. Stepwise transition from the Eocene greenhouse to the Oligocene icehouse. Nat. Geosci. 1, 329–334.

Luo, Z., Su, Q., Wang, Z., Heermance, R.V., Garzione, C., Li, M., Ren, X., Song, Y., Nie, J., 2017. Orbital forcing of Plio-Pleistocene climate variation in a Qaidam Basin lake based on paleomagnetic and evaporite mineralogic analysis. Palaeogeogr. Palaeoclimatol. Palaeoecol. http://dx.doi.org/10.1016/j.palaeo.2017.09.022.

Meng, J., McKenna, M.C., 1998. Faunal turn overs of Paleogene mammals from the Mongolian Plateau. Nature 394, 364–367.

Miller, K.G., Browning, J.V., Aubry, M.P., Wade, B.S., Katz, M.E., Kulpecz, A.A., Wright, J.D., 2008. Eocene-Oligocene global climate and sea-level changes: St. Stephens Quarry, Alabama. Geol. Soc. Am. Bull. 120, 34–53.

Moore, D.M., Reynolds, R.C., 1989. X-ray Diffraction and the Identification and Analysis of Clay Minerals. Oxford University Press, Oxford, pp. 332.

Nie, J., Song, Y., King, J.W., Fang, X., Heil, C., 2010. HIRM variations in the Chinese red-clay sequence: insights into pedogenesis in the dust source area. J. Asian Earth Sci. 38, 96–104.

Nie, J., Garzione, C., Su, Q., Liu, Q., Zhang, R., Heslop, D., Necula, C., Zhang, S., Song, Y., Luo, Z., 2017. Dominant 100,000-year precipitation cyclicity in a late Miocene lake from northeast Tibet. Sci. Adv. 3, e1600762.

Pagani, M., Huber, M., Liu, Z., Bohaty, S.M., Henderiks, J., Sijp, W., Krishnan, S., DeConto, R.M., 2011. The role of carbon dioxide during the onset of Antarctic glaciation. Science 334, 1261–1264.

Pearson, P.N., McMillan, I.K., Wade, B.S., Jones, T.D., Coxall, H.K., Bown, P.R., Lear, C.H., 2008. Extinction and environmental change across the Eocene-Oligocene boundary in Tanzania. Geology 36, 179–182.

Pearson, P.N., Foster, G.L., Wade, B.S., 2009. Atmospheric carbon dioxide through the Eocene-Oligocene climate transition. Nature 461, 1110–1113.

Petruk, W., 1964. Determination of the heavy atom content in chlorite by means of the X-ray diffractometer. Am. Mineral. 49, 61–71.

Prothero, D.R., 1999. Does climatic change drive mammalian evolution? GSA Today 9, 1–7.

Retallack, G.J., 1992. Paleosols and changes in climate and vegetation across the Eocene/Oligocene boundary. In: Prothero, D.R., Berggren, W.A. (Eds.), Eocene-Oligocene Biotic and Climatic Evolution. 1992. Princeton: Princeton University Press, pp. 382–398.

Rudnick, R.L., Fountain, D.M., 1995. Nature and composition of the continental crust: a lower crustal perspective. Rev. Geophys. 33, 267–309.

Scher, H.D., Bohaty, S.M., Zachos, J.C., Delaney, M.L., 2011. Two-stepping into the icehouse: East Antarctic weathering during progressive ice-sheet expansion at the Eocene-Oligocene transition. Geology 39, 383–386.

Song, B., Zhang, K., Lu, J., Wang, C., Xu, Y., 2013. The middle Eocene to early Miocene integrated sedimentary record in the Qaidam Basin and its implications for paleoclimate and early Tibetan Plateau uplift. Can. J. Earth Sci. 50, 183–196.

Sun, X.J., Wang, P.X., 2005. How old is the Asian monsoon system? Palaeobotanical records from China. Palaeogeogr. Palaeoclimatol. Palaeoecol. 222, 181–222.

Sun, J.M., Ni, X.J., Bi, S.D., Wu, W.Y., Ye, J., Meng, J., Windley, B.F., 2014. Synchronous turnover of flora, fauna, and climate at the Eocene-Oligocene Boundary in Asia. Sci. Rep. 4, 7463.

Taylor, S.R., McLennan, S.M., 1985. The Continental Crust: Its Composition and Evolution. Blackwell Scientific Publication, Oxford.

Wang, C.W., Hong, H.L., Song, B.W., Yin, K., Li, Z.H., Zhang, K.X., Ji, J.L., 2011. The early-Eocene climate optimum (EECO) event in the Qaidam basin, northwest China: clay evidence. Clay Miner. 46, 649–661.

Wang, C., Hong, H., Li, Z., Yin, K., Xie, J., Liang, G., Song, B., Song, E., Zhang, K., 2013. The Eocene-Oligocene climate transition in the Tarim Basin, Northwest China: evidence from clay mineralogy. Appl. Clay Sci. 74, 10–19.

Wang, H., Rahn, M., Zhou, J., 2018. Tectonothermal evolution of the Triassic flysch in the Bayan Har Orogen, Tibetan Plateau. Tectonophysics 723, 277–287.

Weaver, C.E., 1989. Clays, Muds, and Shales: Development in Sedimentology. Vol. 44 Elsevier, Amsterdam.

Weaver, C.E., Pollard, L.D., 1973. The Chemistry of Clay Minerals: Development in Sedimentology. Vol. 15 Elsevier, Amsterdam.

Wilson, M.J., 1987. A Handbook of determinative methods in clay mineralogy. In: Blackie. Chapman and Hall.

Wolfe, J.A., 1992. Climatic, floristic, and vegetational changes near the Eocene/Oligocene boundary in North America. In: Prothero, D.R., Berggren, W.A. (Eds.), Eocene-Oligocene Biotic and Climatic Evolution. 1992. Princeton University, Press, Princeton, pp. 421–436.

Wronkiewicz, D.J., Condie, K.C., 1987. Geochemistry of Archean shales from the Witwatersrand Supergroup, South Africa: source-area weathering and provenance. Geochim. Cosmochim. Acta 51, 2401–2416.

Xiao, G.Q., Abels, H.A., Yao, Q.Z., Dupont-Nivet, G., Hilgen, F.J., 2010. Asian aridification linked to the first step of the Eocene-Oligocene climate Transition (EOT) in obliquity-dominated terrestrial records (Xining Basin, China). Clim. Past 6, 501–513.

Yang, Y., Fang, X., Appel, E., Galy, A., Li, M., Zhang, W., 2013. Late Pliocene-Quaternary evolution of redox conditions in the western Qaidam paleolake (NE Tibetan Plateau) deduced from Mn geochemistry in the drilling core SG-1. Quat. Res. 80, 586–595.

Ye, C., Yang, Y., Fang, X., Zhang, W., 2016. Late Eocene clay boron-derived paleosalinity in the Qaidam basin and its implications for regional tectonics and climate. Sediment. Geol. 346, 49–59.

Yin, A., Dang, Y.Q., Wang, L.C., Jiang, W.M., Zhou, S.P., Chen, X.H., Gehrels, G.E., McRivette, M.W., 2008. Cenozoic tectonic evolution of Qaidam basin and its surrounding regions (part 1): the southern Qilian Shan-Nan Shan thrust belt and northern Qaidam basin. Geol. Soc. Am. Bull. 120, 813–846.

Zachos, J.C., Quinn, T.M., Salamy, K.A., 1996. High-resolution (10^4 years) deep-sea foraminiferal stable isotope records of the Eocene-Oligocene climate transition. Paleoceanography 11, 251–266.

Zachos, J., Pagani, M., Sloan, L., Thomas, E., Billups, K., 2001. Trends, rhythms, and aberrations in global climate 65 Ma to present. Science 292, 686–693.

Zanazzi, A., Kahn, M.J., MacFadden, B.J., Terry Jr., D.O., 2007. Large temperature drop across the Eocene-Oligocene transition in central North America. Nature 445, 639–642.

Zeng, L., Wang, L.S., Xu, H.X., Jiao, G.N., Cui, S.N., Han, H., Zhang, B.S., 2010. SY/T 5163-2010. Analysis Method for Clay Minerals and Ordinary Non-clay Minerals in Sedimentary Rocks by the X-ray Diffraction. Petroleum Industry Publishing House, Beijing (in Chinese).

Zhang, W.L., 2006. Cenozoic Uplift of the Tibetan Plateau: Evidence From High Resolution Magnetostratigraphy of the Qaidam Basin. Lanzhou University (PhD Thesis).

Zhang, P., 2015. Magnetostratigraphy and Paleoenvironmental Evolution of the Middle Eocene-Early Miocene Deposits in the Lanzhou Basin, Northwest China. University of Chinese Academy of Sciences (PhD Thesis).

Zhang, C., Guo, Z., 2014. Clay mineral changes across the Eocene-Oligocene transition in the sedimentary sequence at Xining occurred prior to global cooling. Palaeogeogr. Palaeoclimatol. Palaeoecol. 411, 18–29.

Zhang, R., Kravchinsky, V.A., Yue, L., 2012. Link between global cooling and mammalian transition across the Eocene-Oligocene boundary in the continental interior of Asia. Int. J. Earth Sci. 101, 2193–2200.